A Godunov-type finite-volume solver for nonhydrostatic Euler equations with a time-splitting approach

Farshid Nazari[1,2] and **Ramachandran D. Nair[1]**

[1]Institute for Mathematics Applied to Geosciences, National Center for Atmospheric Research, Boulder, Colorado, USA, [2]Advanced Study Program, National Center for Atmospheric Research, Boulder, Colorado, USA

Abstract A two-dimensional conservative nonhydrostatic (NH) model based on the compressible Euler system has been developed in the Cartesian (x, z) domain. The spatial discretization is based on a Godunov-type finite-volume (FV) method employing dimensionally split fifth-order reconstructions. The model uses the explicit strong stability-preserving Runge-Kutta scheme and a split-explicit method. The time-split approach is generally based on the split-explicit method, where the acoustic modes in the Euler system are solved using small time steps, and the advective modes are treated with larger time steps. However, for the Godunov-type FV method this traditional approach is not trivial for the Euler system of equations. In the present study, a new strategy is proposed by which the Euler system is split into three modes, and a multirate time integration is performed. The computational efficiency of the split scheme is compared with the explicit one using the FV model with various NH benchmark test cases.

1. Introduction

Due to the availability of petascale supercomputing resources, there is a new trend in developing global atmospheric models based on computationally intense nonhydrostatic (NH) dynamics. The finite-volume (FV) approach emerged as a method of choice for discretization in such models [e.g., *Tomita et al.*, 2008; *Skamarock et al.*, 2012]. FV is one of the most popular approaches for solving atmospheric equations of motion at all scales because of its inherent conservation, computational economy, and geometric flexibility; in addition, being a *local* method, it offers excellent parallel efficiency. Traditionally, FV models rely on staggered grid system with at least a second-order spatial accuracy. Extending this approach to higher-order accuracy with grid staggering is cumbersome, especially on curvilinear or unstructured grids. Recently, high-order unstaggered FV schemes are introduced for solving NH equations as described in *Ullrich and Jablonowski* [2012] and *Li et al.* [2013], which are based on so-called "Godunov-type" methods.

A large class of FV methods for solving hyperbolic conservation laws are based on high-order extensions of the classical Godunov scheme [*Godunov*, 1959], often referred to as the Godunov-type schemes [*van Leer*, 1979; *Collela and Woodward*, 1984]. Although upwind-based Godunov-type FV methods are very popular in computational fluid dynamics, they have been used for atmospheric NH modeling only recently [e.g., *Ahmad and Lindeman*, 2007; *Norman et al.*, 2011; *Ullrich and Jablonowski*, 2012; *Li et al.*, 2013; *Yang and Cai*, 2014]. A Godunov-type method typically does not rely on staggered grids, and the cell-averaged solution is not assumed to be continuous across the cell (control volume) edges. The discontinuity of the fluxes at the cell interface is resolved by a Riemann solver (numerical flux). This mechanism provides an efficient way to apply FV method for complex grid system including grid adaptivity [*Toro*, 1999]. For the present study, we consider an upwind-based Godunov-type FV method (hereafter referred to as FV method) for solving fully compressible Euler system of equations on a rectangular 2-D (x, z)-domain. The fluxes at the cell interface are reconstructed by fifth-order accurate schemes based on the PQM (piecewise quartic method) [*White and Adcroft*, 2008]. The AUSM$^+$-up (advection upstream splitting method) [*Liou*, 2006] numerical flux is used for the FV model, which is particularly effective for low Mach number problems such as NH atmospheric modeling [*Ullrich and Jablonowski*, 2012; *Chen et al.*, 2013; *Yang and Cai*, 2014].

A major challenge for NH modeling is to develop a practical time stepping method. This is because of the wider spectrum of spatial and temporal scales present in the atmosphere, encompassing fast sound and

gravity wave propagation as well as the slower advection. The high-aspect ratio between horizontal and vertical grid-spacing combined with fast-moving acoustic waves impose a stringent stability constraint on explicit time stepping. This makes the problem computationally very challenging. Although the explicit Runge-Kutta scheme is robust and accurate, it is not an efficient choice for NH modeling because the stringent CFL (Courant-Friedrichs-Lewy) stability restriction associated with acoustic waves and relatively tiny grid-spacing (Δz) in the vertical direction force very small time steps. There are several ways to circumvent this difficulty by employing implicit or semi-implicit type time integration procedures as described in *Durran* [1999]. Specifically, horizontally explicit and vertically implicit (HEVI) time integration strategy [*Weller et al.*, 2013] is a practical option, and adopted for high-order FV [*Ullrich and Jablonowski*, 2012] and discontinuous Galerkin methods [*Bao et al.*, 2015]. Implicit-explicit (IMEX) temporal integration is another choice as recently tested in *Kopera and Giraldo* [2014], *Durran and Blossey* [2012], and *Bourchtein and Bourchtein* [2009].

However, an important advantage of explicit time stepping schemes is their simplicity and high parallel efficiency due to locality with minimal communications between processors when solving the equations of motion. A common strategy to take the advantages of explicit schemes with enhanced computational efficiency is a splitting approach in which the equations of motion are split into fast-slow components. The time step size is then restricted by the CFL number of the low-frequency modes since smaller time steps are applied for the integration of the high-frequency modes. The classical split-explicit method [*Skamarock and Klemp*, 1994; *Wicker and Skamarock*, 2002] is based on this philosophy, which is used for operational NH models [*Tomita et al.*, 2008; *Skamarock et al.*, 2012]. A class of multirate split-explicit time integration methods can be found in *Wensch et al.* [2009]. They further developed these split-explicit methods in terms of stability and accuracy in *Knoth and Wensch* [2014] through optimization algorithms.

In general, the split-explicit time integration methods are based on splitting the equations into fast and slow modes [see e.g., *Wicker and Skamarock*, 2002].

However, for a Godunov-type FV method, it is not obvious to separate each component of the Euler system and perform split-explicit time integration. In this study, a three-way splitting approach is proposed based on the scale analysis in the atmosphere [*Klein*, 2010]. The atmospheric NH system of equations is split into slow, fast-forward, and fast-backward equations. The forward-backward treatment is very popular in atmospheric models, either in split-explicit [*Wicker and Skamarock*, 2002; *Klemp et al.*, 2007] or IMEX [*Weller et al.*, 2013; *Lock et al.*, 2014] schemes. Generally, in a sequential computation of the model variables, the updated velocity will be available for use in pressure calculation.

The model is then evaluated by some well-known NH test cases and the results are compared with the reference solution using the strong stability-preserving third-order Runge-Kutta (SSP-RK3) [*Gottlieb et al.*, 2001] scheme. Computational efficiency of the model is also discussed. Note that for a split-explicit method, the issue with small vertical grid-spacing is handled by an implicit approach as used in HEVI methods [*Tomita et al.*, 2008]. We do not address this in the present work.

The remainder of the paper is organized as follows. In section 2, the NH FV model is described, section 3 deals with various time integration methods. Results with numerical experiments are provided in section 4, followed by summary and conclusions in section 5.

2. The Nonhydrostatic FV Model

2.1. 2-D Euler System
The model is designed to simulate the two-dimensional (2-D) airflow over a rectangular (x, z) domain. The compressible nonhydrostatic Euler system of equations can be written in the following vector form [*Bao et al.*, 2015]:

$$\frac{\partial \rho}{\partial t} + \nabla \cdot (\rho \mathbf{u}) = 0$$

$$\frac{\partial \rho \mathbf{u}}{\partial t} + \nabla \cdot (\rho \, \mathbf{u} \otimes \mathbf{u} + p \, \mathbf{I}) = -\rho g \, \mathbf{k},$$

(1)

$$\frac{\partial \rho \theta}{\partial t} + \nabla \cdot (\rho \theta \, \mathbf{u}) = 0$$

where ρ is the air density, $\mathbf{u} = (u, w)^T$ the velocity vector with the vertical component $w = \mathbf{u} \cdot \mathbf{k}$, and p is the pressure, g is the acceleration due to gravity, and $\mathbf{I}$ represents the 2 $\times$ 2 identity matrix. The potential

temperature θ is related to the real temperature T by $\theta = T(p_0/p)^{R_d/c_p}$. The above system is closed by the equation of state, $p = C_0(\rho\theta)^\gamma$ where $C_0 = R_d^\gamma p_0^{-R_d/c_v}$. The reference surface pressure $p_0 = 10^5$ Pa, and the other thermodynamic constants are given by $\gamma = c_p/c_v$, $R_d = 287$ J kg^{-1} K^{-1}, $c_p = 1004$ J kg^{-1} K^{-1}, $c_v = 717$ J kg^{-1} K^{-1}.

For NH atmospheric modeling, it is customary to write the thermodynamic variables (ψ) as the sum of the mean-state or reference state $\bar\psi$ and the perturbation ψ',

$$\psi(x, z, t) = \bar\psi(z) + \psi'(x, z, t); \quad \psi \in \{\rho, \theta, p, \rho\theta\}, \tag{2}$$

such that the mean-state satisfies the hydrostatic balance,

$$\frac{d\bar p}{dz} = -\bar\rho g. \tag{3}$$

The mean-state part of the thermodynamic variables makes no contribution to the dynamics, and the dynamic processes are triggered and influenced by the perturbation part [see *Clark*, 1977]. When the hydrostatically balanced mean-state is *removed* from the Euler system of equations, the resulting perturbed system can be written in the following vector form as a hyperbolic conservation law:

$$\frac{\partial U}{\partial t} + \frac{\partial F(U)}{\partial x} + \frac{\partial G(U)}{\partial z} = S(U) \quad \Rightarrow \quad \frac{\partial U}{\partial t} + \nabla \cdot \mathbf{F}(U) = S(U), \tag{4}$$

where

$$U = \begin{bmatrix} \rho' \\ \rho u \\ \rho w \\ (\rho\theta)' \end{bmatrix}, \quad F = \begin{bmatrix} \rho u \\ \rho u^2 + p' \\ \rho uw \\ \rho u\theta \end{bmatrix}, \quad G = \begin{bmatrix} \rho w \\ \rho wu \\ \rho w^2 + p' \\ \rho w\theta \end{bmatrix}, \quad S = \begin{bmatrix} 0 \\ 0 \\ -\rho' g \\ 0 \end{bmatrix}, \tag{5}$$

where U is the state vector of conserved quantities, $\mathbf{F} = (F, G)$ is the flux vector with components F and G along x and z directions, respectively, and S is the source term.

2.2. Finite-Volume Discretization

Consider the two-dimensional conservation law (4) on a rectangular domain $\mathcal{D}$, with initial condition $U(x, z, t=0) = U_0(x, z)$, and with appropriate boundary conditions. The domain is partitioned into nonoverlapping $N_x \times N_z$ cells $I_{ij} = [x_{i-1/2}, x_{i+1/2}] \otimes [z_{j-1/2}, z_{j+1/2}]$, where $i = 1, 2, \ldots, N_x$ and $j = 1, 2, \ldots N_z$. Let Δx and Δz be uniform grid-spacings along the x and z directions, respectively, such that $|I_{ij}| = \Delta x \Delta z$. For a cell-centered FV approach, the prognostic variables are treated as cell averages ($\bar U$), which are constants within each cell and discontinuous at the cell interfaces in general. To advance the cell averages at the new time level, FV methods require a reconstruction procedure for fluxes at the cell interfaces from the neighboring cell averages. The cell-averaged conserved quantity $\bar U_{ij}$ on a cell I_{ij} is defined to be

$$\bar U_{ij} = \frac{1}{\Delta x \Delta z} \int_{x_{i-1/2}}^{x_{i+1/2}} \int_{z_{j-1/2}}^{z_{j+1/2}} P_{ij}(x, z) \, dx \, dz, \tag{6}$$

where $P_{ij}(x, z)$ is a piecewise polynomial function that approximates the solution $U(x, z, t)$ on I_{ij}, for a targeted order of accuracy at a given time. $P_{ij}(x, z)$ is also known as the reconstruction function and provides the subgrid scale distribution for U on each cell I_{ij}. Integrating (4) on I_{ij}, and employing the divergence theorem and the conservation constraint (6) leads to the following semidiscretized form:

$$\frac{d}{dt} \bar U_{ij} = \frac{-1}{\Delta x \Delta z} \left[\sum_{e=1}^{4} \int_{\Gamma_e} \mathbf{F} \cdot \mathbf{n} \right] + \bar S_{ij}, \tag{7}$$

where Γ_e is the boundary wall for the cell I_{ij}, $\mathbf{n}$ is the unit outward normal vector on Γ_e, $\mathbf{F}$ is the flux function, and $\bar S_{ij}$ is the cell-averaged source term.
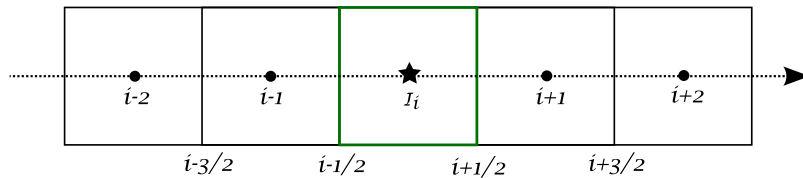
Figure 1. The five-point compact computation stencil used for 1-D reconstructions, where cell "i" is located at the center. The cell centers are marked by dots and indices $i, i\pm1, i\pm2$; and the cell interfaces (edges) are marked with indices $i\pm1/2, i\pm3/2$.

The formal order of accuracy of a FV scheme obtained from (7) is tied up with that of the reconstruction function P_{ij} and the flux integral. High-order multidimensional FV schemes can be rigorously derived by using a high-order polynomial approximation for U, combined with a consistent Gauss quadrature for the flux integrals along the cell boundaries [*Shu*, 1997]. However, such FV schemes are computationally prohibitive for many practical applications including 3-D NH modeling. For the sake of computational efficiency and algorithmic simplicity, we consider a relatively simple FV formulation of (7). The complexity of a fully 2-D reconstruction can be significantly reduced by a "dimension-by-dimension" approach involving 1-D reconstruction in each coordinate direction as described in *Katta et al.* [2015]. An advantage of this approach is that only one numerical flux evaluation is required per cell wall, resulting in a significant computational saving. Nevertheless, a major drawback is that the formal order of accuracy of FV scheme degrades to second-order in certain cases even though high-order 1-D reconstructions are employed.

The semidiscretized form (7) can be further simplified as follows:

$$\frac{d}{dt}\bar{U}_{ij} = -\left[\frac{\hat{F}_{i+1/2,j}-\hat{F}_{i-1/2,j}}{\Delta x} + \frac{\hat{G}_{i,j+1/2}-\hat{G}_{i,j-1/2}}{\Delta z}\right] + \bar{S}_{ij}, \tag{8}$$

where $\hat{F}_{i\pm1/2,j}$ and $\hat{G}_{i,j\pm1/2}$ are the numerical fluxes evaluated at the cell interfaces as shown in Figure 1. Since the reconstructed solution is discontinuous across the cell interface, the flux is not uniquely defined. The discontinuity is resolved by replacing normal flux **F** with a numerical flux $\hat{\mathbf{F}}=\hat{\mathbf{F}}(U^-, U^+)$, by means of a Riemann solver [*Toro*, 1999]; which combines the fluxes corresponding to the left (U^-) and right (U^+) states of the discontinuous solution (U) at the cell interface. For example, the Rusanov (or local Lax-Friedrichs) flux at the cell interface can be written as:

$$\hat{\mathbf{F}}(U^-, U^+) \cdot \mathbf{n} = \frac{1}{2}\left[\mathbf{F}(U^-)\cdot\mathbf{n}+\mathbf{F}(U^+)\cdot\mathbf{n}-\alpha_{\max}(U^+-U^-)\right], \tag{9}$$

where $\alpha_{\max}$ is the maximum absolute value of eigenvalues of the flux Jacobian $\mathbf{F}'(U)$. For the Euler system (1), $\alpha_{\max}=\max\left\{|v^-|+c_s, |v^+|+c_s\right\}$, where $c_s=\sqrt{\gamma R_d T}$ is the speed of sound and $v=\mathbf{u}\cdot\mathbf{n}$. A wide variety of Riemann solvers are available with varying computational complexity such as Roe, HLLC, etc. [*Toro*, 1999], which are traditionally developed for the gas dynamics applications.

The Rusanov flux (9) is simple to implement and popular in discontinuous Galerkin methods, however, for FV cases it is too diffusive and rarely used for practical applications. Since the Mach number associated with NH dynamics is relatively small, an upwind-based flux recipe designed for low Mach number is more appropriate. The Riemann solver AUSM$^+$-up [*Liou*, 2006] developed for all Mach numbers gaining prominence for NH modeling. We adopt the AUSM$^+$-up flux for the FV solver and the details are given in the Appendix A.

2.3. 1-D Reconstruction Schemes

The reconstruction process is one of the most important ingredients of a FV discretization because it dictates the accuracy, efficiency, and nonoscillatory properties of the scheme. As described above, we are interested in high-order 1-D reconstruction scheme cast in a dimension-by-dimension approach for the 2-D Euler solver. The fifth-order accurate Piecewise Quartic Method (PQM) introduced in *White and Adcroft* [2008] has several computationally attractive features including simplicity, flexibility with variable grid-spacing and optional monotonicity. We consider the PQM approach for reconstructing fluxes at the cell edges.

The reconstructing polynomial $P_i(x)$ has the following generic form for a cell "i":

$$P_i(x) = a_0 + a_1 x + a_2 x^2 + a_3 x^3 + a_4 x^4, \quad \frac{1}{\Delta x} \int_{x_{i-1/2}}^{x_{i+1/2}} P_i(x)\, dx = \bar{U}_i, \tag{10}$$

where the coefficients $a_k, k = 0, \ldots, 4$, are uniquely determined using five constraints involving the left and right edge values $U_{i-1/2} = U(x_{i-1/2})$ and $U_{i+1/2} = U(x_{i+1/2})$, respectively, and the derivatives (for details see *White and Adcroft* [2008]). The edge value estimates of the approximate solution for a cell i can be computed from the neighboring cell averages, using the five-point stencil schematically shown in Figure 1, as below

$$U_{i-1/2} = \frac{1}{60}(-3\bar{U}_{i-2} + 27\bar{U}_{i-1} + 47\bar{U}_i - 13\bar{U}_{i+1} + 2\bar{U}_{i+2}), \tag{11}$$

$$U_{i+1/2} = \frac{1}{60}(2\bar{U}_{i-2} - 13\bar{U}_{i-1} + 47\bar{U}_i + 27\bar{U}_{i+1} - 3\bar{U}_{i+2}). \tag{12}$$

To compute the numerical flux $\hat{F}_{i+1/2,j}$ in (8) requires the left (U^-) and right (U^+) edge values at the interface $x_{i+1/2}$, and can be obtained from equations (11) and (12). Similarly the numerical flux in z direction $\hat{G}_{i,j+1/2}$ can be computed.

3. Time Integration

The semidiscretized Euler system (8) leads to a system of ordinary differential equations (ODE) and can be written in the following general form,

$$\frac{d}{dt} U(t) = \mathcal{L}(U) \quad \text{in} \quad (0, T), \tag{13}$$

where U is the approximate solution and $\mathcal{L}$ is the operator associated with FV spatial discretization. The above ODE can be solved by a variety of solvers. We consider the SSP-RK3 scheme [*Gottlieb et al.*, 2001] as a basic explicit time stepping method for the reference solution and the third-order Runge-Kutta (RK3) scheme [*Wicker and Skamarock*, 2002] as a basis for split-explicit time stepping method as follows:

SSP-RK3:

$$U_{(1)} = U_n + \Delta t \mathcal{L}(U_n), \tag{14}$$

$$U_{(2)} = \frac{3}{4} U_n + \frac{1}{4} U_{(1)} + \frac{1}{4} \Delta t \mathcal{L}(U_{(1)}), \tag{15}$$

$$U_{n+1} = \frac{1}{3} U_n + \frac{2}{3} U_{(2)} + \frac{2}{3} \Delta t\, \mathcal{L}(U_{(2)}), \tag{16}$$

RK3:

$$U_{(1)} = U_n + \frac{1}{3} \Delta t \mathcal{L}(U_n), \tag{17}$$

$$U_{(2)} = U_n + \frac{1}{2} \Delta t \mathcal{L}(U_{(1)}), \tag{18}$$

$$U_{n+1} = U_n + \Delta t\, \mathcal{L}(U_{(2)}), \tag{19}$$

where n and $n + 1$ indicate time level at t_n and $t_{n+1} = t_n + \Delta t$. The CFL limit for the explicit time stepping is $C\,\Delta t/h \leq 1$, where $h = \min\{\Delta x, \Delta z\}$, and C is the maximum speed of the system.

3.1. Scale Separation Overview
Scale separation is inherently featured in the atmosphere both in time and space [*Klein*, 2010]. Time scales in atmospheric flows range significantly from microseconds to weeks or more. Effective and efficient

modeling needs to consider this fact. According to the scale study on the atmospheric flows by *Klein* [2010], different ratios can be observed for different variables. Regarding the velocity, the atmosphere can be decoupled into three wave speed regimes: sound speed (c_s), internal wave speed (c_{int}), and convective wind velocity (u_w) with the typical following ratios:

$$c_{int}/c_s \sim 1/3 \sim \varepsilon^{1/2}, \ u_w/c_{int} \sim 1/9 \sim \varepsilon, \ \text{and} \ u_w/c_s \sim \varepsilon^{3/2},$$

where ε is a dimensionless parameter. These ratios show that the atmospheric flow equations are stiff because of the large ratios between the waves propagation speeds, which are used in the following stability analysis (section 3.2.2).

3.2. Time-Splitting Approach

In this study, fully compressible nonhydrostatic Euler equations are solved through a split-explicit time integration method. Following the RK3, split-explicit method in *Wicker and Skamarock* [2002], the same time integration method with some modifications is used in the proposed splitting framework.

3.2.1. Time-Splitting ODE

Based on the multiple scales discussed above, we consider an ordinary differential equation with three terms:

$$\dot{y} = s(y) + f_f(y) + f_b(y) \tag{20}$$

in which s, f_f, and f_b represent the slow (nonstiff), fast-forward, and fast-backward terms, respectively. The time-split method is based on RK3 scheme (17)–(19) with n_s number of micro-time steps; i.e., $\Delta\tau = \Delta t/n_s$. In other words, the large time step Δt, is divided to n_s smaller micro-time steps, $\Delta\tau$. The slow terms are calculated using the large time step at each RK stage, while the fast terms are calculated using the number of micro-time steps in each RK stage in the forward-backward framework. It means that the slow term is first calculated using the last RK stage y value. Then the small steps start with the slow term frozen at its last updated value. In the small step loop, the fast-forward and fast-backward terms are updated sequentially until the loop is completed.

The split-explicit scheme is applied to (20) as follows:

$$\tilde{y}_{(stage)}^{\tau+\Delta\tau} = y_{(stage)}^{\tau} + [s(y_{(stage)-1}) + f_f(y_{(stage)}^{\tau})]\Delta\tau$$
$$y_{(stage)}^{\tau+\Delta\tau} = \tilde{y}_{(stage)}^{\tau+\Delta\tau} + f_b(\tilde{y}_{(stage)}^{\tau+\Delta\tau})\Delta\tau, \tag{21}$$

where $y_{(stage)}$ denotes the value of y at the RK3 stages and is used as a loop inside each RK3 stage. Note that $y_{(stage)}^{\tau=t_n} = y_n$ and $y_{n+1} = y_{(3)}$. There are $n_s/3$, $n_s/2$, and n_s loops for the first, second, and third RK3 stage, respectively.

Our implementation of the three-way splitting is described as follows:

Stage 1:
The loop at the first RK3 stage is

$$\tilde{y}_{(1)}^{\tau+\Delta\tau} = y_{(1)}^{\tau} + [s(y_n) + f_f(y_{(1)}^{\tau})]\Delta\tau$$
$$y_{(1)}^{\tau+\Delta\tau} = \tilde{y}_{(1)}^{\tau+\Delta\tau} + f_b(\tilde{y}_{(1)}^{\tau+\Delta\tau})\Delta\tau, \tag{22}$$

for $n_s/3$ micro-time steps. Thus at the end of the loop, $y_{(1)}$ is obtained at time $t_n + \Delta t/3$.

Stage 2:
In the RK3 method, the advance from the first-stage ($t_n + \Delta t/3$) to the second stage ($t_n + \Delta t/2$) is $\Delta t/6$, with $n_s/6$ microsteps. This means that when $n_s = 6$, the advance equals $\Delta\tau$ (which is the case in this study). Hence, we advance $y_{(1)}$ only by one microstep ($\Delta\tau$) at the second stage:

$$\tilde{y}_{(2)} = y_{(1)} + [s(y_{(1)}) + f_f(y_{(1)})]\Delta\tau$$
$$y_{(2)} = \tilde{y}_{(2)} + f_b(\tilde{y}_{(2)})\Delta\tau. \tag{23}$$

Note that there is no superscript for $y_{(1)}$, $\tilde{y}_{(2)}$, and $y_{(2)}$, which indicates (23) is a one-time calculation reducing the computational effort.
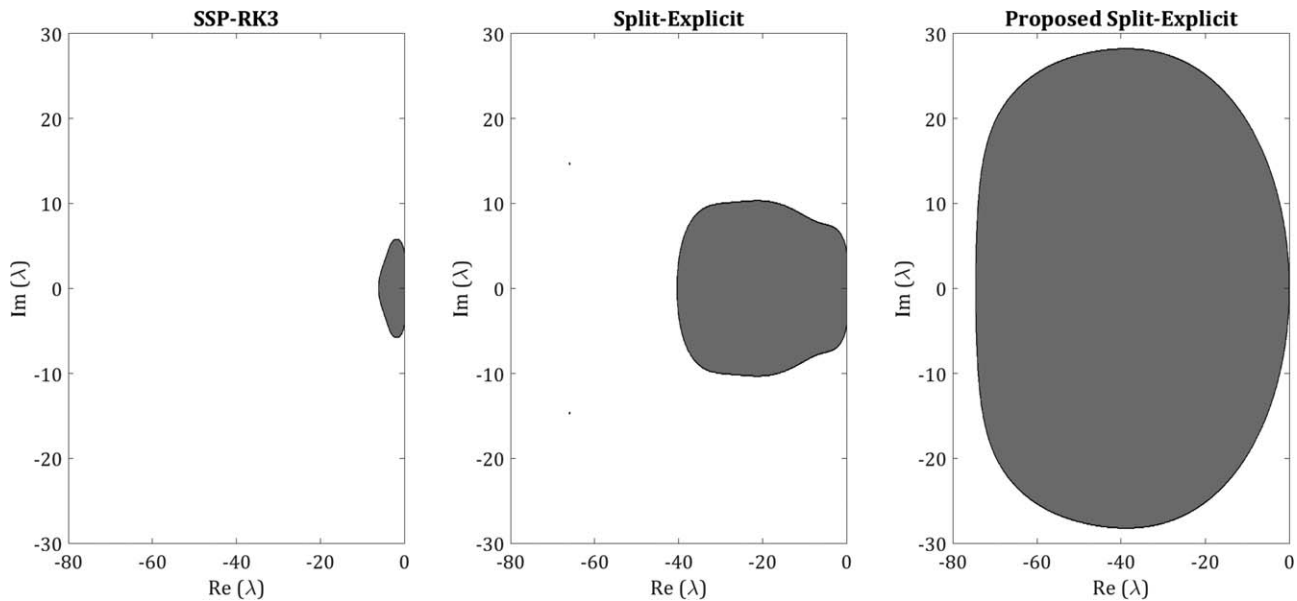
Figure 2. Stability (dark) regions of the SSP-RK3, the full split-explicit and the proposed split-explicit schemes for $s = 1$, $f_f = 10$, and $f_b = 30$.

Stage 3:
Finally, at the third RK3 stage, we will have

$$\tilde{y}_{(3)}^{\tau+\Delta\tau} = y_{(3)}^{\tau} + [s(y_{(2)}) + f_f(y_{(3)}^{\tau})]\Delta\tau$$

$$y_{(3)}^{\tau+\Delta\tau} = \tilde{y}_{(3)}^{\tau+\Delta\tau} + f_b(\tilde{y}_{(3)}^{\tau+\Delta\tau})\Delta\tau.$$

(24)

At the end of this loop, y_{n+1} is obtained.

Still, one can use the full split-explicit with $n_s/2$ number of microsteps at the second stage in a similar way to the other stages.

3.2.2. Stability and Accuracy Analysis

For stability analysis of the time integration methods, the standard ordinary differential equation $\dot{y} = \lambda y$ is considered [see *Butcher*, 2008] but with three terms as in (20):

$$\dot{y} = (s + f_f + f_b)\lambda y,$$

(25)

where λ is the complex variable. Plots of the related stability regions are shown in Figure 2 for the ratios of wave speeds in the atmosphere (see section 3.1) with $s = 1$, $f_f = 10$, and $f_b = 30$ with the step size 0.01. The dark area shows the region of stability. It is clearly observed that the proposed split-explicit scheme has much larger stability region, which suggests the stability preservation for larger time steps when the equation is stiff. The atmospheric system of equations is a totally nonlinear problem with both real and imaginary eigenvalues. The eigenvalue analysis of the resulting equations shows that the eigenvalues consist of both real and imaginary parts with large values [see *Klemp et al.*, 2007]. So a scheme with a larger stability region along the real axis is certainly desirable, especially when it is shown that the imaginary stability is considerably increasing as it gets farther from the imaginary axis. This is also proved in the benchmark tests in section 4.

As an alternative, one can use the full split-explicit scheme where we get at least the same imaginary stability as SSP-RK3 (Figure 2, middle plot).

Similar discussion exists for the order of accuracy. As can be seen in Figure 3, the order of accuracy for the full split-explicit scheme is as the same as RK3 when there is no fast terms ($f_f = f_b = 0$), while the proposed scheme is second-order accurate. As soon as the fast terms appear in the problem, there is no difference in the order of accuracy between the modified and full split schemes; both are first-order accurate. Similarly in the tests in section 4, we hardly see any difference in the stability and accuracy of the results using the two schemes. However, using the full split scheme results in approximately 10% computational saving, while the modified scheme gives about 25%.
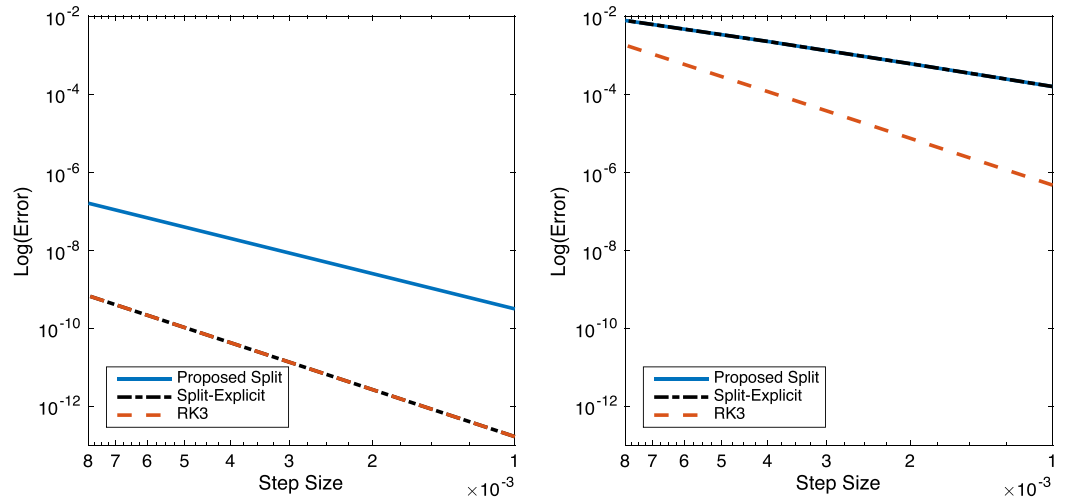
Figure 3. Order of accuracy comparison among the same schemes as in Figure 2 for (left) $s = 1$, $f_f = 0$, and $f_b = 0$ and (right) $s = 1$, $f_f = 10$, and $f_b = 30$.

3.2.3. Implementation to the 2-D Euler System

As discussed in section 3.2.1, the 2-D Euler system (5) can be split into three subsystems of slow (nonstiff), fast-forward, and fast-backward equations.

$$U_s = \begin{bmatrix} 0 \\ \rho u \\ \rho w \\ 0 \end{bmatrix}, \quad F_s = \begin{bmatrix} 0 \\ \rho u^2 \\ \rho uw \\ 0 \end{bmatrix}, \quad G_s = \begin{bmatrix} 0 \\ \rho wu \\ \rho w^2 \\ 0 \end{bmatrix}, \quad S_s = \begin{bmatrix} 0 \\ 0 \\ 0 \\ 0 \end{bmatrix}; \tag{26}$$

$$U_f = \begin{bmatrix} \rho' \\ 0 \\ 0 \\ (\rho\theta)' \end{bmatrix}, \quad F_f = \begin{bmatrix} \rho u \\ 0 \\ 0 \\ \rho u\theta \end{bmatrix}, \quad G_f = \begin{bmatrix} \rho w \\ 0 \\ 0 \\ \rho w\theta \end{bmatrix}, \quad S_f = \begin{bmatrix} 0 \\ 0 \\ 0 \\ 0 \end{bmatrix}; \tag{27}$$

$$U_b = \begin{bmatrix} 0 \\ \rho u \\ \rho w \\ 0 \end{bmatrix}, \quad F_b = \begin{bmatrix} 0 \\ p' \\ 0 \\ 0 \end{bmatrix}, \quad G_b = \begin{bmatrix} 0 \\ 0 \\ p' \\ 0 \end{bmatrix}, \quad S_b = \begin{bmatrix} 0 \\ 0 \\ -\rho'g \\ 0 \end{bmatrix}. \tag{28}$$

Using the notations introduced in section 3.2.1, we replace y by U, s by the slow (F_s, G_s, and S_s) terms, f_f by the fast-forward (F_f, G_f, and S_f) terms, and f_b by the fast-backward (F_b, G_b, and S_b) terms. Analogous to the split scheme (21), the Euler system (26)–(28) is integrated as follows:

$$\tilde{U}^{\tau+\Delta\tau}_{(stage)} = U^\tau_{(stage)} + [F^x_s(U_{(stage)-1}) + G^z_s(U_{(stage)-1}) + S_s(U_{(stage)-1})$$
$$+ F^x_f(U^\tau_{(stage)}) + G^z_f(U^\tau_{(stage)}) + S_f(U^\tau_{(stage)})]\Delta\tau \tag{29}$$

$$U^{\tau+\Delta\tau}_{(stage)} = \tilde{U}^{\tau+\Delta\tau}_{(stage)} + [F^x_b(U^\tau_{(stage)}) + G^z_b(U^\tau_{(stage)}) + S_b(U^\tau_{(stage)})]\Delta\tau.$$

As in (21), this is the loop inside each RK3 stage. Superscripts "x" and "z" represent discrete partial derivatives in "x" and "z" directions, respectively. Since the U vector has always two components zero, we only need to use
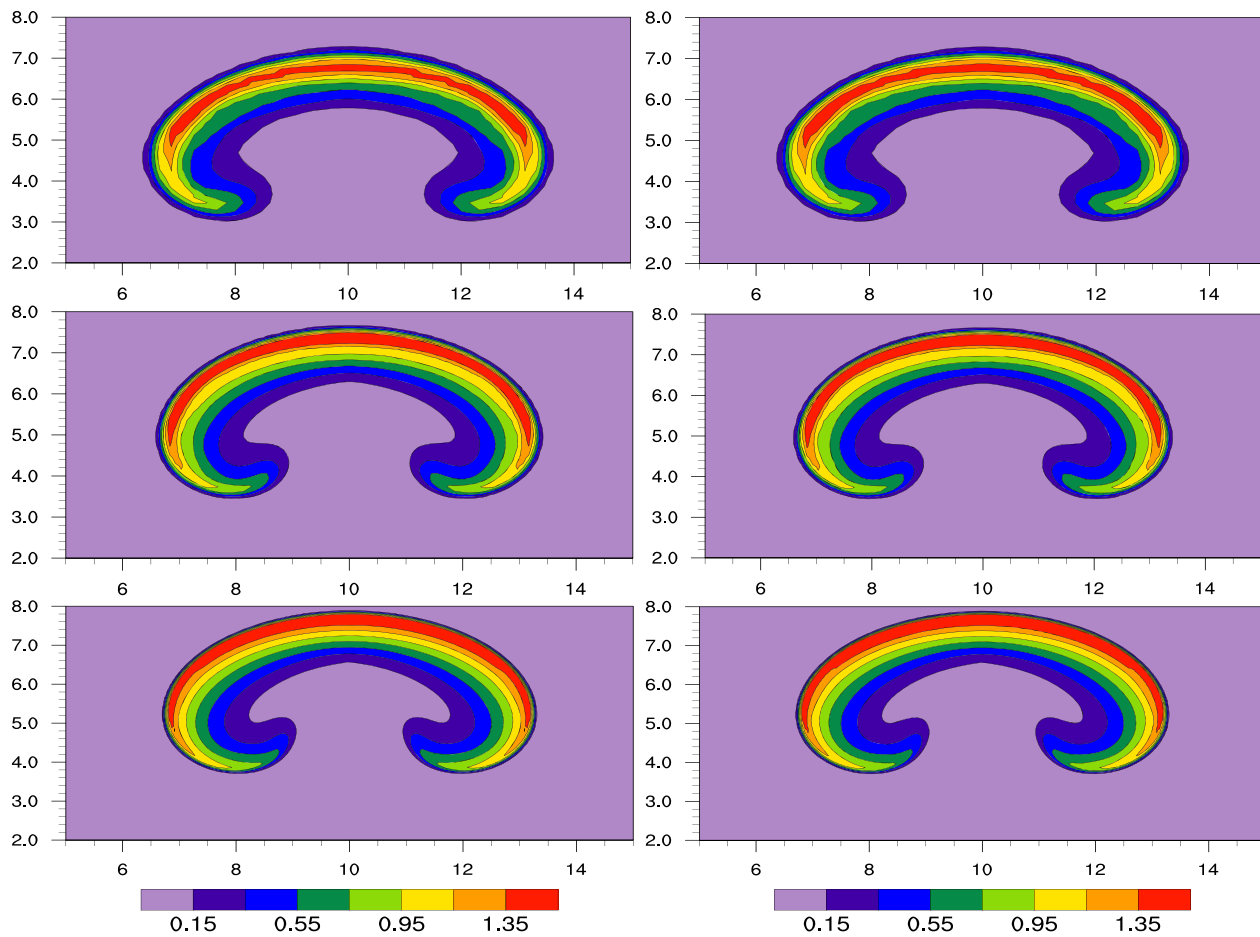
Figure 4. Potential temperature perturbation for the rising thermal bubble test at time $t = 1000$ s with the resolutions of $\Delta z = \Delta x = 200, 100$, and 50 m from the top to bottom. The results with SSP-RK3 and proposed split-explicit schemes are shown in the left and the right columns, respectively. The time step used in the split-explicit is 5 times that of the SSP-RK3 which is $\Delta t = 0.4$ s, at the coarsest resolution and is inversely proportional to the grid-spacing to keep the CFL number constant.

the edge value reconstruction (with PQM) for those components that have been updated immediately before the current calculations. In other words, the edge value reconstruction is implemented for two components of U instead of four. In each loop, reconstructed values of the conservative variables can be reused in the solution process. In (27) only U_f is updated, so the PQM is only used for the U_f nonzero components before calculating the fluxes in (27). Similarly, when U_b is updated in (28), the PQM is used only for the U_b nonzero components. In this way, the total number of the reconstruction which is the most expensive part in the computations is four.

Besides, before calculating the fluxes in the slow equation, which is only calculated once at each RK3 stage, the edge value reconstruction is used only for the U_b nonzero components. The reason is that the U_f nonzero components have already been updated before calculating the fast-backward fluxes.

It is worth mentioning that one can swap (27) and (28) without significant differences in the results, which means calculating (28) forward and (27) backward.

4. Numerical Experiments

For setting up the initial and boundary conditions for the FV solver with various NH benchmark tests, we follow the strategy used in *Bao et al.* [2015] and *Li et al.* [2013], and the details are omitted.

4.1. Rising Warm Bubble

The rising convective thermal bubble test case is widely used for evaluating time stepping methods for NH models [*Wicker and Skamarock*, 2002; *Ahmad and Linedman*, 2007]. The thermal bubble is warmer than the
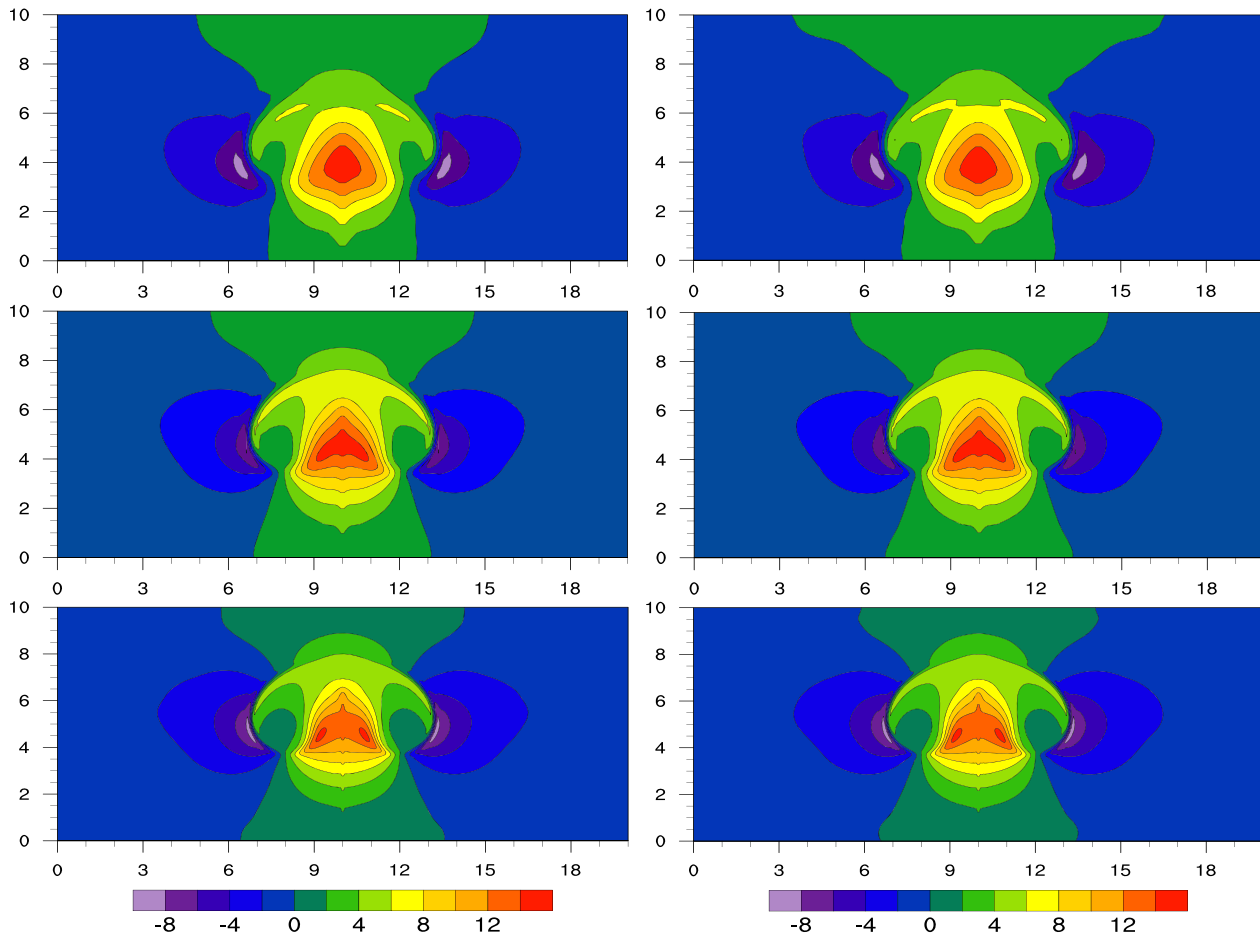
Figure 5. Same as in Figure 4 but for the vertical velocity (w).

ambient air therefore, it rises while deforming as a result of the shearing motion caused by the wind gradients. Larger gradients occur at the upper part of the bubble and eventually it reshapes into a mushroom cloud. The convective thermal bubble test uses a hydrostatic balance with a uniform potential temperature, $\bar{\theta}(z) = 300$ K. The following perturbation is added to hydrostatic background $\bar{\theta}$ to trigger the vertical motion:

$$\theta' = \theta'_c \max(0, 1 - d/r_c), \tag{30}$$

where $\theta'_c = 2$ K, $r_c = 2$ km, and $d = \sqrt{(x - x_c)^2 + (z - z_c)^2}$ in which $x_c = 10$ km and $z_c = 2$ km. The domain is 20 km × 10 km with no-flux boundary conditions. No artificial diffusion is applied, and no analytic solution is available for this test.

The comparison of the two schemes is shown in Figure 4. The results are very similar although the time step in the proposed split scheme is 5 times the SSP-RK3's. The split scheme, hence, shows good performance with increased computational efficiency of ~25%. Likewise, the vertical velocity in Figure 5 shows the same behavior. The results are comparable with that shown in *Li et al.* [2013] with a high-order FV model, but the FV-PQM evolution is smoother.

In order to examine the mass conservation of the proposed splitting scheme, time history of the normalized mass error is shown in Figure 6. As can be seen, the model conserves mass to the machine precision ($O(10^{-15})$) for both SSP-RK3 and split schemes.

4.2. Inertia-Gravity Wave Test

The NH inertia-gravity wave test introduced by *Skamarock and Klemp* [1994] is an effective tool to verify the accuracy of various time stepping schemes in a more realistic NH setting. The test consists of a channel
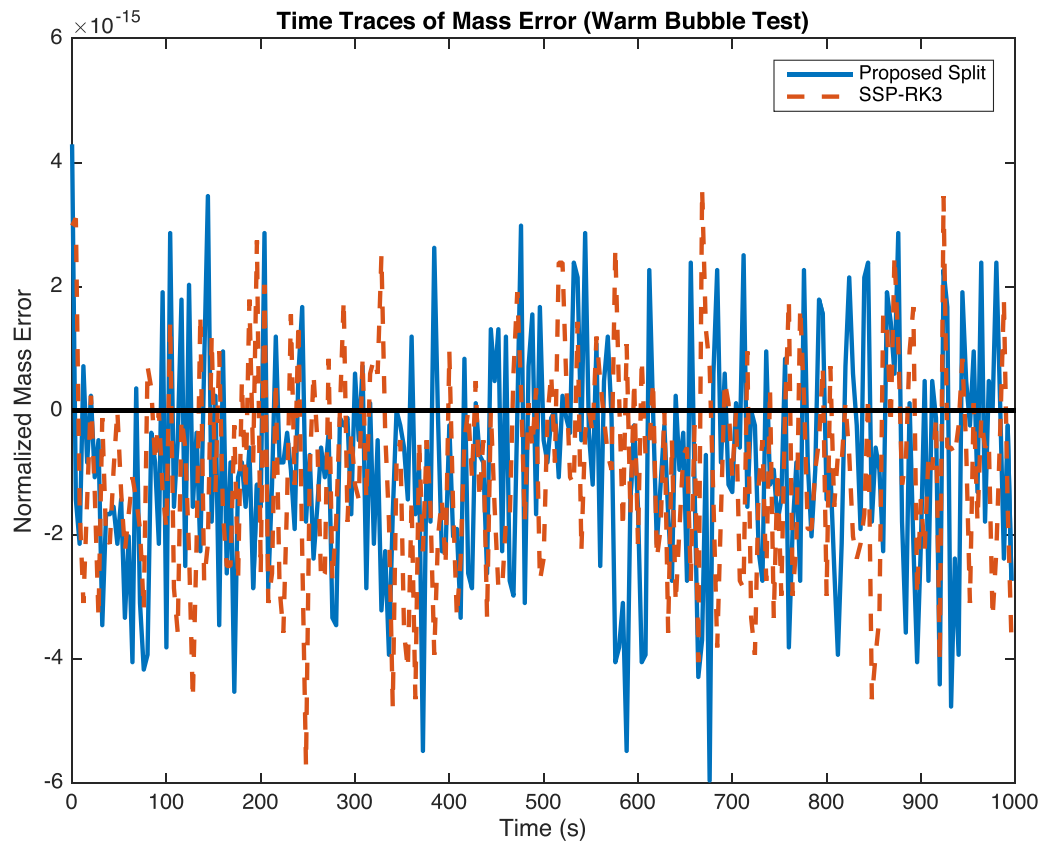
Figure 6. The time traces of normalized mass error for SSP-RK3 and the proposed split schemes for the warm bubble test with $\Delta x = \Delta z = 200$ m.

with a uniform advection velocity where a perturbation in potential temperature is applied in the middle. This perturbation then propagates through the channel, both left and right, but is influenced by the mean advection velocity. The test parameters and initial condition are the same as *Skamarock and Klemp* [1994]. The Brunt-Väisälä frequency is $N_f = 10^{-2}$ s^{-1}, the upper boundary is placed at $z_T = 10$ km, the perturbation half-width is $a_m = 5$ km, and the initial horizontal velocity is $u = 20$ m s^{-1}. The inertia-gravity waves are excited by an initial potential temperature perturbation (θ') of the following form:

$$\theta' = \theta'_c \frac{a_m^2 \sin(\pi z / h_c)}{a_m^2 + (x - x_c)^2}, \quad (31)$$

where $\theta'_c = 0.01$ K, $h_c = 10$ km, and $x_c = 100$ km. The domain is [0, 300] $\times$ [0, 10] km^2, with the periodic lateral boundary condition and no-flux at the top and bottom boundaries. The simulation time is $t_T = 3000$ s. The results are compared for the two schemes in Figure 7, with the aspect ratio of $\Delta x / \Delta z = 10$ for $\Delta z = 100$ and 200 m.

The time step for the SSP-RK3 scheme is $\Delta t = 0.4$ s. The results again admit that the split scheme performs satisfactorily in comparison with the SSP-RK3. It shows almost no difference between the results, while we obtain about 25% saving in computational cost with the split-explicit scheme. This is again corroborated by the comparison between the two schemes in Figure 8, where the potential temperature perturbation (θ') is plotted at $z = 5$ km through the channel. The values of θ' are symmetric about $x = 160$ km, and they are very similar that the differences are hardly distinguishable.

Furthermore, the error comparison between the two schemes is implemented for θ' and vertical velocity in Figure 9. Both schemes are approaching second-order convergence as the resolution increases. Negligible differences exist between the convergence rates so the results are barely distinguishable.
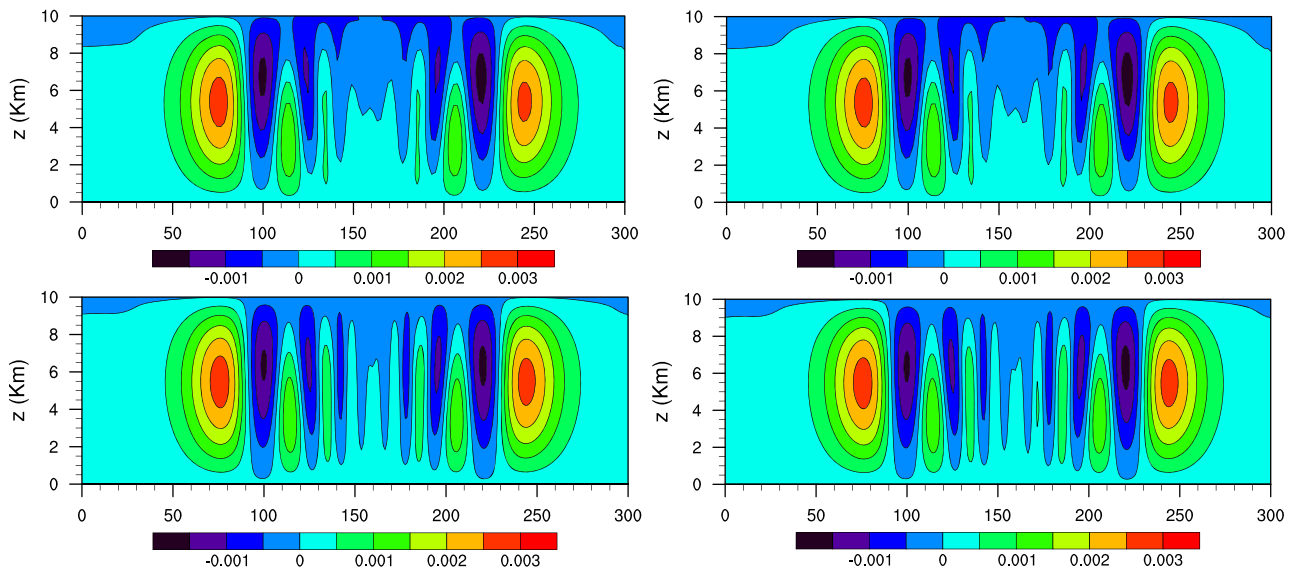
Figure 7. Potential temperature perturbation for the Inertia Gravity Wave test at time $t = 3000$ s with the resolutions of (top) $\Delta z = 200$ m and (bottom) $\Delta z = 100$ m. $\Delta x = 10\Delta z$. The results with SSP-RK3 and the proposed split-explicit are shown in the left and right plots, respectively. The time step used in the split-explicit is 4.6 times the time step used in SSP-RK3, which is $\Delta t = 0.4$ s.

4.3. Density Current (Straka) Test

The density current test by *Straka et al.* [1993] is another benchmark to evaluate the performance of numerical schemes in NH atmospheric models. Contrary to the thermal bubble test, a cold bubble drops into a neutrally stratified atmosphere and starts to propagate forward. The forward motion of the cold flow results in shear at the top that produces Kelvin-Helmholtz instability rotors. The atmosphere has the uniform potential temperature of $\bar{\theta} = 300$ K at the hydrostatic balance initially, where the following perturbation is introduced:

$$\theta(x,z) = \begin{cases} \bar{\theta}(z) & \text{if } r > 1 \\ \bar{\theta}(z) + \theta'_c \left[1 + \cos(\pi r)\right], & \text{otherwise} \end{cases}.$$

where $\theta'_c = -15$ K, $r = \sqrt{[(x-x_c)/x_r]^2 + [(z-z_c)/z_r]^2}$, $(x_c, z_c) = (0, 3)$ km, $(x_r, z_r) = (4, 2)$ km. A dynamic viscosity of $v = 75$ m^2 s^{-1}, is applied at all resolutions as recommended in *Straka et al.* [1993]. The model is integrated for 900 s on a domain $[-26.5, 26.5] \times [0, 6.4]$ km^2 with no-flux boundary conditions.

First, we show the advantage of using AUSM$^+$-up flux as opposed to Rusanov (9) flux with the density current simulations. In Figure 10, the results with AUSM$^+$-up and Rusanov numerical fluxes are shown in the top and bottom plots, after 900 s at a resolution of $\Delta z = \Delta x = 100$ m. Because of the excessive diffusion
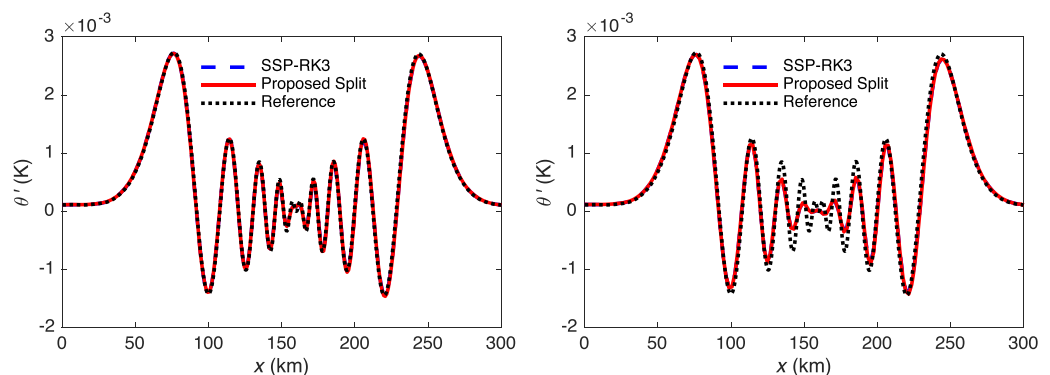

Figure 8. Potential temperature perturbation comparison as in Figure 7 at the height of $z = 5$ km. (left) $\Delta z = 100$ m and (right) $\Delta z = 200$ m. The reference solution time step is $\Delta t = 0.04$ s with $\Delta z = 50$ m.
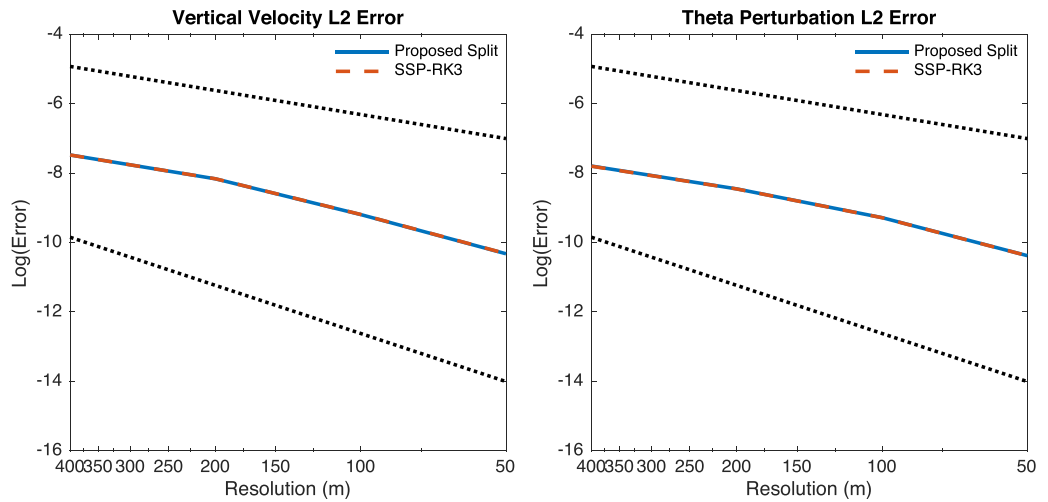
Figure 9. L2-error comparison of SSP-RK3 and the proposed split-explicit for the Inertia Gravity Wave test. For the reference solution, $\Delta z =$ 25 m and $\Delta t = 0.02$ s with $\Delta x = 10\Delta z$. The grid size and the time step double up to 400 m. The dotted lines are first and second-order convergence rates.

inherent with the Rusanov flux, the solution appears more smooth and failed to capture the fine features Kelvin-Helmholtz rotors. The solution with AUSM$^+$-up at the same resolution shows more details of the rotors, and comparable to other published results [*Bao et al.*, 2015]. Computational cost for these two schemes is comparable.

The results for the proposed time-split method and SSP-RK3 at three different resolutions of $\Delta z = \Delta x =$ 200, 100, and 50 m are presented in Figure 11. They are similar qualitatively capturing the three Kelvin-Helmholtz rotors for all the resolutions. Still, the split scheme seems better resolving the flow features for the coarsest resolution with 5 times larger time step. The results are qualitatively comparable with other published high-order models results [*Li et al.*, 2013; *Ullrich and Jablonowski*, 2012].
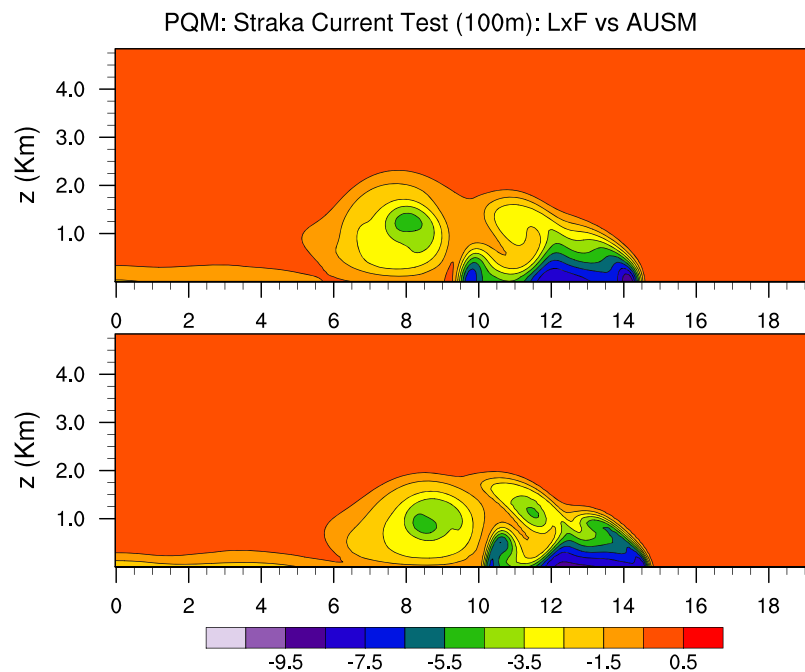

Figure 10. The simulated results for the Straka density current test at time 900 s with the FV model. The top plot shows potential temperature perturbation (θ') with the Rusunov flux (9), and the bottom plot shows the same but with the AUSM$^+$-up numerical flux. The model is configured with a resolution $\Delta z = \Delta x = 100$ m, and explicit time step $\Delta t = 0.25$ s.
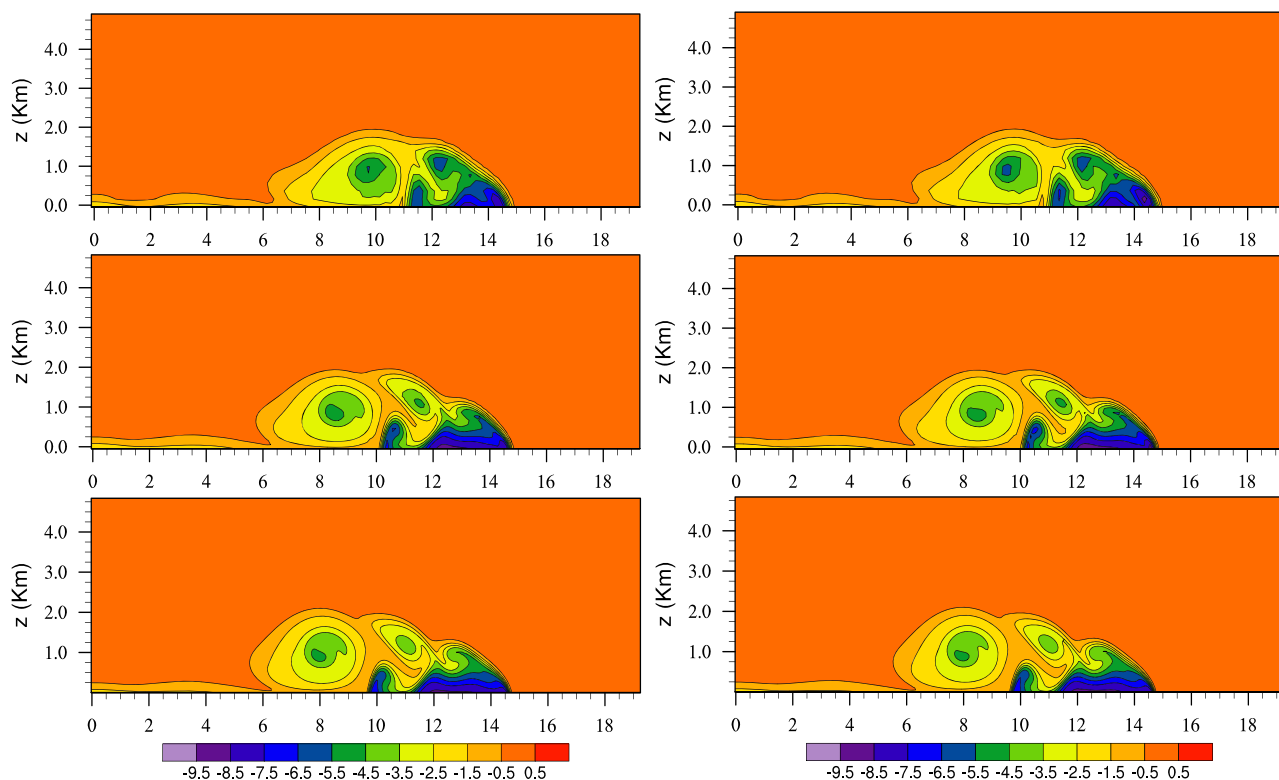
Figure 11. Potential temperature perturbation for the density current test at time $t = 900$ s with the resolutions of $\Delta z = \Delta x = 200, 100,$ and 50 m from top to bottom. The time step used in the proposed split-explicit is 5 times the time step used in SSP-RK3 which is $\Delta t = 0.5$ s, at the coarsest resolution and is inversely proportional to the grid-spacing to keep the CFL number constant. SSP-RK3 in the left and the split-explicit in the right.

To compare the two schemes quantitatively, Table 1 includes different run details and the results at the maximum possible time step for each scheme. It is shown that $\sim$25% computational saving is obtained using the split scheme. The longitudinal profile of the potential temperature perturbation at the height of $z = 1.2$ km is shown in Figure 12, where the three Kelvin-Helmholtz rotors are represented by the three valleys. The results of the split and SSP-RK3 schemes are in close agreement. As the resolution increases, finer features of the current are resolved, which reflects the multiscale nature of the flow. This is obvious in Figure 11 as well.

5. Summary and Conclusions

A Godunov-type finite-volume (FV) atmospheric model with a new time-splitting method has been developed. The model solves the fully compressible nonhydrostatic (NH) Euler system. The FV solver takes the advantages of fifth-order piecewise quartic method (PQM) reconstructions in the spatial discretization. For computational economy, the reconstruction scheme is implemented in a dimensionally split way. The numerical flux (Riemann solver) recipe used for the FV solver is based on the AUSM^{+}-up (advection upstream splitting method) flux, which is particularly effective for low Mach number problems as is in the NH modeling.

Table 1. Comparison of SSP-RK3 and the Time-Splitting Method for the Straka Density Current Test at the Maximum Possible Time Step

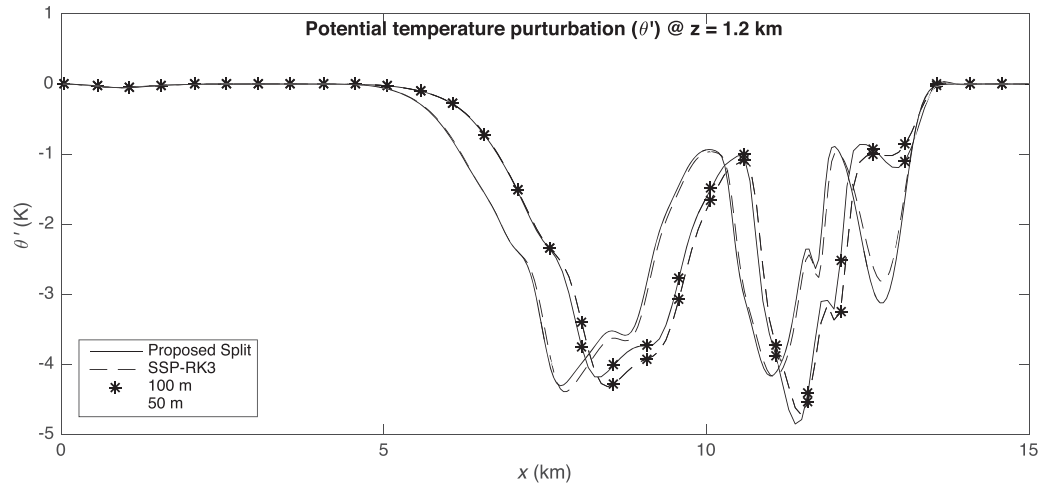| Scheme	$\Delta z = \Delta x$ (m)	Δt (s)	min (θ') (K)	max (θ') (K)	CPU Time (s)
SSP-RK3	50	0.125	-8.82	1.27×10^{-2}	1524.87
Split-explicit	50	0.625	-8.87	4.10×10^{-2}	1155.98
SSP-RK3	100	0.25	-8.78	8.82×10^{-2}	169.90
Split-explicit	100	1.25	-9.01	1.56×10^{-1}	134.16
SSP-RK3	200	0.5	-8.39	1.53×10^{-1}	20.41
Split-explicit	200	2.5	-9.31	2.00×10^{-1}	15.17

Figure 12. Potential temperature perturbation as in Figure 11 at the height of $z = 1.2$ km for the two resolutions of $\Delta z = \Delta x = 100$ (asterisk) and 50 (no marker) m. The proposed split-explicit is the solid line and SSP-RK3 is the dashed line.

Traditionally for a split-explicit method, the acoustic modes in the Euler system are solved using small time steps while the advective modes are treated with larger time steps. However, for the Godunov-type FV method this traditional approach is not trivial for the Euler system of equations, because each component of the system is coupled through the Riemann solver. The proposed time-split approach consists of three modes and the Euler system is split into slow, fast-forward, and fast-backward equations to represent these modes. The ODE stability analysis confirms much larger stability region for the split scheme, which suggests using of noticeably larger time steps without facing instability issues. It is numerically shown that the new splitting scheme does not violate conservation properties. The computational efficiency of the split scheme is compared with the explicit method, using the FV model with various NH benchmark test cases. The proposed split scheme is about 25% more efficient. The FV model performs well under the standard benchmark tests, and the results are qualitatively comparable with other published high-order FV results. The small vertical grid-spacing and vertically propagating acoustic mode results in stringent CFL restriction with explicit time stepping. This issue is circumvented by an implicit approach in the vertical direction so that the overall CFL restriction is limited by horizontal grid-spacing. For the present study, we do not include the implicit part, although the work in this direction is in progress. Our goal is to extend the 2-D FV model to a 3-D framework including topography.

Appendix A: AUSM$^+$-Up Flux

Since we consider the FV discretization in orthogonal (x, z) coordinates, the implementation of AUSM$^+$-up flux [*Liou*, 2006] can be directly described in terms of the Euler system (5) in x direction, where the state vector $U = (\rho', \rho u, \rho w, (\rho\theta)')^T$ and the flux $F = (\rho u, \rho u^2 + p', \rho uw, \rho u\theta)^T$. As introduced in section 2.2, the left and right states of a variable ψ at the cell interface is indicated by ψ^- and ψ^+, respectively. In order to describe the algorithm briefly, we employ the notations as used in *Yang and Cai* [2014]. The AUSM-family of fluxes requires a decomposition of the inviscid flux into convective (advective) and pressure fluxes:

$$\hat{F}(U^-, U^+) = \hat{F}_{con}(U^-, U^+) + \hat{F}_{prs}(U^-, U^+), \tag{A1}$$

and the averaged quantities at the interface such as the density $\dot{\rho} = (\rho^- + \rho^+)/2$, and sound speed $\dot{c} = (\sqrt{\gamma p^-/\rho^-} + \sqrt{\gamma p^+/\rho^+})/2$. The local Mach numbers at the interface are $m^\pm = u^\pm/\dot{c}$, such that the average Mach number $\dot{m}$ satisfies $\dot{m}^2 = ((m^-)^2 + (m^+)^2)/2$. Then the interface Mach number can be defined as

$$\dot{m} = \mathcal{M}_4^+(m^-) + \mathcal{M}_4^-(m^+) - \frac{K_p}{f_a} \max\left(1 - \sigma \dot{m}^2, 0\right) \frac{(p^+)' - (p^-)'}{\dot{\rho}\,\dot{c}^2}, \tag{A2}$$

where

$$\mathcal{M}_4^{\pm}(m) = \begin{cases} \dfrac{1}{2}(m \pm |m|) & \text{if } |m| \geq 1 \\ \mathcal{M}_2^{\pm}(m)\left[1 \mp 16\,\beta\,\mathcal{M}_2^{\mp}(m)\right], & \text{otherwise} \end{cases}, \tag{A3}$$

where $\mathcal{M}_2^{\pm}(m) = (m \pm 1)^2/4$. Note that split Mach numbers $\mathcal{M}_k^{\pm}$ are polynomial functions of degree $k = 2, 4$ [*Liou*, 2006]. Now the convective component of the flux in (A1) is defined as:

$$\hat{F}_{con}(U^-, U^+) = \begin{cases} \dot{c}\,\dot{m}\,(1, u^-, w^-, \theta^-)^T & \text{if } \dot{m} > 0 \\ \dot{c}\,\dot{m}\,(1, u^+, w^+, \theta^+)^T, & \text{otherwise} \end{cases}. \tag{A4}$$

In order to find the pressure component in (A1), the pressure perturbation at the interface $\dot{p}'$ is required which is defined by

$$\dot{p}' = \mathcal{P}_5^+(m^-)\,(p^-)' + \mathcal{P}_5^-(m^+)\,(p^+)' - K_u\,f_a\,\mathcal{P}_5^+(m^-)\,\mathcal{P}_5^-(m^+)(\rho^- + \rho^+)\,\dot{c}\,(u^+ - u^-), \tag{A5}$$

where

$$\mathcal{P}_5^{\pm}(m) = \begin{cases} \dfrac{1}{2}\left[1 \pm \text{sign}(m)\right] & \text{if } |m| \geq 1 \\ \mathcal{M}_2^{\pm}(m)\left[(\pm 2 - m) \mp 16\alpha\, m\, \mathcal{M}_2^{\mp}(m)\right], & \text{otherwise} \end{cases}. \tag{A6}$$

The pressure component of (A1) is obtained from the following relation,

$$\hat{F}_{prs}(U^-, U^+) = F(0, \dot{p}', 0, 0). \tag{A7}$$

Following *Liou* [2006], the free parameters used in (A2) and (A5) are set to be $K_p = 1/4$, $K_u = 3/4$, $f_a = \sigma = 1$, $\alpha = 3/16$, and $\beta = 1/8$. Thus, (A4) and (A7) together constitute the AUSM$^+$-up numerical flux $\hat{F}(U^-, U^+)$ in x direction, similarly $\hat{G}(U^-, U^+)$ in z direction can be computed.

References

Ahmad, N., and J. Linedman (2007), Euler solutions using flux-based wave decomposition, *Int. J. Numer. Methods Fluids*, *54*, 47–72.

Bao, L., R. Klöfkorn, and R. D. Nair (2015), Horizontally Explicit and Vertically Implicit (HEVI) time discretization scheme for a discontinuous Galerkin nonhydrostatic model, *Mon. Weather Rev.*, *143*, 972–990.

Bourchtein, A., and L. Bourchtein (2009), Semi-Lagrangian semi-implicit time-splitting scheme for a regional model of the atmosphere, *J. Comput. Appl. Math.*, *227*(1), 115–125.

Butcher, J. C. (2008), *Numerical Methods for Ordinary Differential Equations*, John Wiley, New York.

Clark, T. L. (1977), A small-scale dynamics model using a terrain-following coordinate transformation, *J. Comput. Phys.*, *24*, 186–215.

Chen, X., N. Andronova, J. E. Penner, J. P. Boyd, C. Jablonowski, and S.-J. Lin (2013), A control-volume model of the compressible Euler equations with a vertical Lagrangian coordinate, *Mon. Weather Rev.*, *141*, 2526–2544.

Collela, P., and P. R. Woodward (1984), The Piecewise Parabolic Method (PPM) for gas-dynamical simulations, *J. Comput. Phys.*, *54*, 174–201.

Durran, D. R. (1999), *Numerical Methods for Wave Equations in Geophysical Fluid Dynamics*, Springer, New York.

Durran, D. R., and P. N. Blossey (2012), Implicit-explicit multistep methods for fast-wave-slow-wave problems, *Mon. Weather Rev.*, *140*(4), 1307–1325.

Godunov, S. K. (1959). A difference method for numerical calculation of discontinuous solution of hydrodynamics, *Mat. Sb. (N.S.)*, *47*(89), 271–306.

Gottlieb, S., C.-W. Shu, and E. Tadmore (2001), Strong stability-preserving high-order time discretization methods, *SIAM Rev.*, *43*, 89–112.

Katta K. K., R. D. Nair, and V. Kumar (2015), High-order finite-volume transport on the cubed sphere: Comparison between 1D and 2D reconstruction schemes, *Mon. Weather Rev.*, *143*, 2947–2954.

Klein, R. (2010), Scale-dependent models for atmospheric flows, *Annu. Rev. Fluid Mech.*, *42*, 249–274.

Klemp, J. B., W. C. Skamarock, and J. Dudhia (2007), Conservative split-explicit time integration methods for the compressible nonhydrostatic equations, *Mon. Weather Rev.*, *135*(8), 2897–2913.

Knoth, O., and J. Wensch (2014), Generalized split-explicit Runge-Kutta methods for the compressible Euler equations, *Mon. Weather Rev.*, *142*, 2067–2081.

Kopera, M. A., and F. X. Giraldo (2014), Analysis of adaptive mesh refinement for IMEX discontinuous Galerkin solutions of the compressible Euler equations with application to atmospheric simulations, *J. Comput. Phys.*, *275*, 92–117.

Li, X., C. Chen, X. Shen, and F. Xiao (2013), A multimoment constrained finite-volume model for nonhydrostatic atmospheric dynamics, *Mon. Weather Rev.*, *141*, 1216–1240.

Liou, M.-S. (2006), A sequel to AUSM. Part II: AUSM$^+$-up for all speeds, *J. Comput. Phys.*, *214*, 137–170.

Lock, S. J., N. Wood, and H. Weller (2014), Numerical analyses of Runge-Kutta implicit-explicit schemes for horizontally explicit, vertically implicit solutions of atmospheric models, *Q. J. R. Meteorol. Soc.*, *140*(682), 1654–1669.

Norman, M. R., R. D. Nair, and F. H. M. Semazzi (2011), A low communication and large time step explicit finite-volume solver for nonhydrostatic atmospheric dynamics, *J. Comput. Phys.*, *230*, 1567–1584.

Shu, C.-W. (1997), Essentially non-oscillatory and weighed essentially non-oscillatory schemes for hyperbolic conservation laws, in *Advanced Numerical Approximation of Nonlinear Hyperbolic Equations, Lecture Notes Math.*, vol. *1697*, edited by A. Quarteroni, pp. 325–432, Springer, Berlin.

Skamarock, W., and J. B. Klemp (1994), Efficiency and accuracy of the Klemp-Wilhelmson time-splitting technique, *Mon. Weather Rev.*, *122*, 2623–2630.

Skamarock, W. C., J. B., Klemp, M. G. Duda, L. D. Flower, S.-H. Park, and T. D. Ringler (2012), A multiscale nonhydrostatic atmospheric model using centroidal voronoi tesselations and c-grid staggering, *Mon. Weather Rev.*, *140*, 3090–3105.

Straka, J. M., R. B. Wilhelmson, L. J. Wicker, J. R. Anderson, and K. K. Droegemeier (1993), Numerical solutions of a nonlinear density current: A benchmark solution and comparisons, *Int. J. Numer. Methods Fluids*, *17*(1), 1–22.

Tomita, H., K. Goto, and M. Satoh (2008), A new approach to atmospheric general circulation model: Global cloud resolving model NICAM and its computational performance, *SIAM J. Sci. Comput.*, *30*, 2755–2776.

Toro, E., (1999), *Riemann Solvers and Numerical Methods for Fluid Dynamics*, Springer, Berlin.

Ullrich, P., and C. Jablonowski (2012), Operator-split Runge-Kutta-Rosenbrock methods for nonhydrostatic atmospheric models, *Mon. Weather Rev.*, *140*, 1257–1284.

van Leer, B. (1979). Towards the ultimate conservative difference scheme—V: A second-order sequel to Godunov's method, *J. Comput. Phys.*, *32*, 101–136.

Weller, H., S.-J. Lock, and N. Wood (2013), Runge-Kutta IMEX schemes for the horizontally explicit/vertically implicit (HEVI) solution of wave equations, *J. Comput. Phys.*, *252*, 365–381.

Wensch, J., O. Knoth, and A. Galant (2009), Multirate infinitesimal step methods for atmospheric flow simulation, *BIT Numer. Math.*, *49*(2), 449–473.

White, L., and A. Adcroft (2008), A high-order finite volume remapping scheme for nonuniform grids: The piecewise quartic method (PQM), *J. Comput. Phys.*, *227*, 7394–7422.

Wicker, L. J., and W. Skamarock (2002), Time splitting methods for elastic models using forward time schemes, *Mon. Weather Rev.*, *130*, 2088–2097.

Yang, C., and X. Cai (2014), A scalable fully implicit compressible Euler solver for mesoscale nonhydrostatic simulation of atmospheric flows, *SIAM J. Sci. Comput.*, *36*, 23–47.